Advanced Photonics Research

ADVANCED PHOTONICS RESEARCH Open Access

www.adpr-journal.com

RESEARCH ARTICLE OPEN ACCESS

Carrier Funneling and Luminescent Collimation for Extreme Diffuse Light Concentration

D. Methorst | E. C. Garnett

AMOLF, Amsterdam, The Netherlands

Correspondence: E. C. Garnett (e.garnett@amolf.nl)

Received: 21 April 2026 | **Revised:** 30 June 2026 | **Accepted:** 13 July 2026

Keywords: diffuse light concentration | directivity | luminescent concentrators | perovskites | photonics

ABSTRACT

Passive (nonabsorbing) lenses are only able to focus direct (collimated) light and therefore cannot concentrate light from the thermodynamic perspective: any decrease in spatial extent must be compensated by an increase in the angular extent of the light beam to satisfy the second law of thermodynamics. In principle, light-absorbing (active) lenses can compensate the increase in brightness (optical concentration) with a decrease in the emitted photon energy (Stokes shift). The performance of such luminescent concentrators falls remarkably short of their thermodynamic potential: all demonstrations of light concentration beyond 4× can improve theoretically by at least a factor of a million. This enormous gap between the thermodynamic and practical limits of light concentration stems from the requirement of emitted light to travel long distances through a strongly absorbing waveguide. Higher concentration factors require longer distances, which unavoidably magnify reabsorption and scattering losses. We propose a novel approach using carrier funneling and luminescent collimation, which decouples concentration from emission propagation distance, breaking the major practical limitation of luminescent concentrators. Finite-difference time-domain, transport and recombination calculations combined with realistic material properties of mixed halide perovskite film/microlens arrays demonstrate concentration factors above 290×, reaching more than 14% of the thermodynamic limit.

1 | Introduction

Focusing light has been a widely used tool in modern science. The earliest scientists developed lenses for telescopes to study the stars and celestial motion [1], opening up the new field of astronomy. Later, the same lenses were implemented in the first optical microscopes, allowing scientists to visualize bacteria and cellular structures, launching the field of microbiology [2]. More recently, light focusing has been at the heart of optical fiber technology, enabling modern telecommunications [3]. Conventional lenses used in all these applications are passive (nonabsorbing), which means that the maximum focusing they can achieve is fundamentally limited by the degree of collimation of the input beam. This restriction arises due to the law of etendue conservation, which is ultimately a consequence of the 2nd law of thermodynamics: the etendue (product of area and solid angle of light beam) is proportional to the photon entropy and therefore cannot be reduced without an energy penalty [4]. Passive optics do not change the photon energy between the input and output beams and therefore must compensate any reduction in area with an equivalent increase in solid angle. This means that standard (nonabsorbing) lenses can focus light (reduce the area while increasing the solid angle), but cannot concentrate light: they cannot increase the brightness (photons $Sr^{-1}m^{-2}s^{-1}eV^{-1}$) of a light source. Equivalently, standard lenses cannot focus diffuse light: since the solid angle of diffuse light cannot be increased, focusing it (reducing the area) reduces the entropy of the light field and thus requires optics that absorb incoming photons and emit them at a lower energy (Stokes shift). Such absorbing lenses are known as luminescent concentrators [5–31] and are the only optical elements suitable for diffuse light focusing or optical concentration more broadly. It is key to realize that while "focusing" and "concentrating" light are

often used interchangeably, they have different meanings in a thermodynamic context. In this manuscript, we will use the thermodynamic definition of concentration (increasing brightness), where focusing only means a reduction in the beam area, without considering changes in the solid angle. Luminescent concentrators have been studied extensively for solar cells (known as luminescent solar concentrators or LSCs) [5–12, 16–31] but are also emerging as an important route toward light sources that combine the high brightness of lasers with the high power of light-emitting diodes for ultrahigh brightness, large-area displays, and projection applications [13–15].

While passive lenses show nearly ideal performance in both their conventional form and the more recent flat lens variety, achieving near-unity numerical aperture values in air [32, 33], luminescent concentrators typically perform many orders of magnitude worse than the thermodynamic limit imposed by their Stokes shift (Table 1) [13–15, 18, 22–31, 35]. Furthermore, while passive lenses can be easily scaled to kilometers to collect more signal without any significant degradation in performance (as is done typically with giant telescope arrays) [36], luminescent concentrator efficiency drops drastically with size, showing a practical collection area limit of one hundred square centimeters [11].

The source of this low efficiency lies in the transverse design: luminescent concentrators absorb incoming light through the thickness of a waveguide (typically glass, plastic, or other transparent matrix) doped with an emitter (typically dye, quantum dot, or other gain medium) and concentrate it by guiding emitted light trapped by total internal reflection in the plane of the waveguide to small collectors at the edges. This implies that conventional luminescent concentrators are effectively using a strongly absorbing waveguide as a focusing lens. Higher concentration factors can only be achieved by increasing the propagation distance through the absorbing waveguide, which unavoidably leads to higher reabsorption and scattering losses.

We propose using localized small bandgap emitters within a larger bandgap matrix to do the electronic concentration by carrier funneling, rather than optical concentration by the luminescent waveguide. After the electronic concentration we use lenses aligned to these localized emitters as collimators. The highly directional luminescence can then be easily focused by any passive lens, which only needs to perform well at a single wavelength (emission peak), facilitating the use of flat lenses and diffractive optics. As we will show, this combined electronic concentration and optical collimation approach has the same thermodynamic limit as standard luminescent concentrators, but the change in absorption/emission symmetry decouples the concentration factor from the emission propagation length. This decoupling enables concentration factors only limited by the Stokes shift of the emitter, diffusion length of photogenerated carriers (funneling distance), and outcoupling efficiency of the collimator, with no performance degradation as a function of diffuse light collector area.

Directional photoluminescence has been widely demonstrated using nanophotonic structures such as Mie resonators [37, 38], metasurfaces [39, 40], photonic crystals [41], and BIC cavities [42], which achieve angular control through resonant dipole–mode coupling, multipolar interference, or symmetry protected high-Q modes. However, none of these techniques satisfy the basic requirements for a practical diffuse light concentrator: nearly complete absorption of incident light over a large spatial, angular, and frequency range. Techniques like free-space collimation where light is absorbed over the full upper hemisphere and emission is redirected in a smaller solid angle are an effective approach to overcome these flaws. Such approaches have recently been demonstrated using plasmonic nanoantenna arrays or a nanophotonic coating to direct the emission into a narrow escape cone, enabling significant etendue reduction [34, 43]. While these approaches demonstrate emission over narrow solid angles, they still have spatially distributed emission throughout the absorbing film, relying on luminescent concentration and the associated reabsorption, escape cone, and scattering losses. To spatially decouple absorption from emission, Förster resonance energy transfer incorporated in LSCs has been explored as well [44]. In that work, dense networks of donor molecules absorb incident light and transfer the excited states to a smaller number of emitting acceptor molecules, which is a form of electronic

TABLE 1 | List of LSCs from literature with specified absorption onset in nm (Abs), PL peak in nm (PL peak), thermodynamic limit for concentration factor (C_{max}), geometric gain (G), achieved concentration factor (C_{ach}) and the ratio of C_{ach} over C_{max} (η_C).

Ref	Abs	PL peak	C_{max}	G	C_{ach}	η_C
[22][a]	650	830	~8.0E + 06	12.5	0.875	1.1E − 07
[23]	540	640	~1.2E + 06	43	4.4	4.2E − 06
[24][a]	500	600	~8.9E + 06	10	6.1	6.8E − 07
[25][a]	460	628	~1.4E + 12	157.2	12.7	9.4E − 12
[26]	500	520	~40	12.5	3.3	8.25E − 2
[27]	784	885	~998	10	2.5	2.5E − 3
[28]	400	550	~1.8E + 14	1.83	0.486	2.6E − 15
[29]	347	454	~1.8E + 14	10	0.41	7.0E − 14
[30]	620	862	~2.3E + 09	35.7	2.89	1.2E − 09
[31]	550	600	~1.4E + 03	10	1.53	1.1E − 6
[34][a]	Not given	650	100[b]	2.5	2	2.0E − 2

[a]Reported values correspond to calculated or simulated performance under idealized conditions.
[b]Thermodynamic limit given by authors calculated using the same methodology as this work.

concentration. Because of the significant Stokes shift and the decoupling between absorption and emission locations, reabsorption losses are reduced. However, in the best case, these systems rely on aligned dipole emitters, with poor directional emission, which still limits their theoretical concentration factor far below what is thermodynamically possible.

The key insight in our architecture is to combine carrier funneling (electronic concentration to localized emitters) with directional emission (optical collimation). This enables near-unity absorption of broadband, fully diffuse light with simultaneous etendue reduction to provide monochromatic, incoherent, and collimated emission that can be focused by conventional lenses. All the previously published advanced nanophotonic techniques for emission control could be leveraged in our approach: future implementations could integrate features such as metasurfaces and photonic crystals to control each of the localized emitters or to increase the outcoupling efficiency.

We first outline the principle behind electronic concentration and optical collimation and map the theoretical limiting performance as a function of Stokes shift, diffusion length, and outcoupling efficiency. We then simulate the performance using a mixed halide perovskite film/microlens array as the absorber and collimator and show that we can achieve concentration factors above 290× (>14% of the thermodynamic limit) with realistic material parameters. Furthermore, our design can be scaled to any size without changing the performance, opening up new possibilities in high-brightness and high-power incoherent light sources for a variety of optoelectronic applications.

2 | Theoretical Framework

2.1 | Definitions and Losses in Diffuse Light Concentration

To compare the performance of current luminescent concentrators and our new luminescent collimator design, we first need to define a few performance metrics and the underlying loss processes. For any optical concentrator, the concentration factor (C) is a product of the geometric gain (G) and the optical efficiency (η_{opt})

$$C = \frac{B_{out}}{B_{in}} = G^{*}\eta_{opt} = \frac{A_{in}\Omega_{in}}{A_{out}\Omega_{out}}{}^{*}\eta_{opt} \tag{1}$$

where C is the brightness (B) ratio, G is the inverse ratio of etendue (A and Ω are the area and solid angle of the beams) and η_{opt} is the photon flux ratio between the output and input light beams. The geometric gain of standard luminescent concentrators is usually defined as the ratio between the area of the surface of the absorbing layer and the sides, because the solid angle of the input and output beams is similar. However, this is not formally correct and in cases where there is a big difference in the angular spread between the input and output beams (as in our design discussed below), this error has important consequences. For a lossless system ($\eta_{opt} = 1$), C and G are equivalent. The optical efficiency can be defined according to underlying loss mechanisms as

$$\eta_{opt} = \eta_{abs}{}^{*}\eta_{PLQY}{}^{*}\eta_{out} \tag{2}$$

where η_{abs} is the light absorption efficiency of the system (fraction of incident light absorbed), η_{PLQY} gives the fraction of absorbed photons that are reemitted at a lower energy and η_{out} gives the fraction of emitted photons that eventually reach the output beam. For most state-of-the-art luminescent concentrators, η_{abs} and η_{PLQY} approach unity, but the optical efficiency is still low because of scattering and (re)emission losses out of the waveguide [16, 17]. Since higher concentration necessarily requires longer waveguiding distances, these loss processes limit the concentration and optical efficiency that can be achieved. Record efficiency luminescent concentrators reported over the past 10 years rarely exceed a concentration factor of 4, and even when they do, their theoretical limit due to the Stokes shift is typically millions of times higher. Table 1 shows a collection of reported luminescent concentrators together with their concentration factor and the corresponding theoretical limit. The poor performance in both absolute concentration achieved and especially that compared to the thermodynamic limit raises the importance of a novel approach to diffuse light concentration. Importantly, the low performance compared to the theoretical limit is inherently limited by designs using luminescent waveguides for optical concentration; previous simulation studies (including the literature depicted in Table 1) have shown that even with ideal optical properties there is a practical efficiency limit that lies on a similar scale to what has been achieved experimentally, far below the thermodynamic limit. This massive gap between the thermodynamic and practical limit of diffuse light concentrators using luminescent concentration in a light-emitting waveguide was already recognized decades ago [4]. Here we provide an alternative approach with a different geometry that breaks this practical limit.

2.2 | Novel Approach: Combining Electronic Concentration With Collimated Emission

Rather than using a light absorbing waveguide to concentrate emission (Figure 1a), our approach electronically concentrates absorbed carriers to a small emission spot within a light-absorbing film, which, when coupled to the focus spot of a lens, allows for collimated emission and ultimately concentration of diffuse light. The overarching principle of our approach requires three steps (Figure 1b). First, diffuse light is absorbed in a semiconducting film, and photogenerated carriers are funneled to small regions within the film that exhibit a lower bandgap. Such carrier funneling processes are widely used to enhance excited state densities for light emission applications, for example in core–shell quantum dots and quantum wells (used in LEDs) [45–47] and have also been observed in phase-segregated mixed halide perovskite films [48]. This carrier funneling already provides the spatial concentration effect, which leads to a lower etendue: the input diffuse light covers a large area and solid angle, while the emitted diffuse light covers the same large solid angle but a smaller area. Second, the confined emitter regions are placed at the focal point of a lens, which collimates the emission. The degree of collimation is determined by the numerical aperture (NA) of the lens as well as the fidelity of alignment between the emitter and the focal point of the lens. Third,

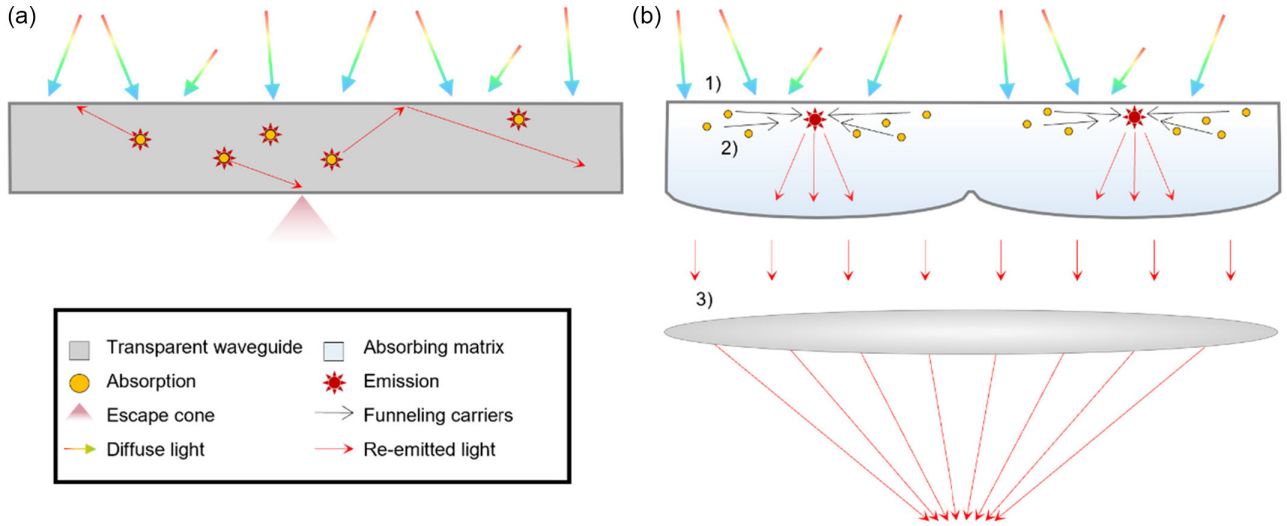

FIGURE 1 | Process of concentration of diffuse light for conventional LSCs (a) and for our approach (b). At step 1, diffuse light is absorbed and excited carriers funnel to the emission region. At step 2, light is emitted and coupled to the photonic design. The interaction between the emitter and the interface can affect the outcoupling of light. At step 3, the collimated light is focused using a standard lens. In our approach the absorption and emission event are spatially separated, while in conventional LSCs these events occur at the same location.

the collimated beam formed from many emitter-lens pairs is focused by an external lens. In these three steps, only the first one requires energy to compensate for the reduction in entropy; steps 2 and 3 are essentially a projection system that can use fully passive optics since they do not change the etendue. Previous work demonstrates the feasibility of step 1 of the mechanism by showing an increased photovoltaic efficiency due to an increase in V_{OC} [49], but lacks the outcoupling of light (step 2) which limits its use for high brightness diffuse light concentration applications. Our approach has both transmissive and reflective implementations, with diffuse light entering through the top and collimated light exciting along the same axis, through either the bottom or through the top.

The difference in symmetry compared to standard LSCs drastically reduces losses and decouples performance from the diffuse light collector size. Because emitted light can couple directly out of the light absorbing film, the reabsorption and scattering losses that degrade LSC performance are avoided, especially at larger concentration factors. Instead, the performance is limited by three factors: (1) the Stokes shift between absorption and emission (approximately the bandgap difference between the absorbing film and the emitting regions), which sets the thermodynamic concentration limit, (2) the diffusion length of carriers required to reach the lower-bandgap emitter regions, which determines how closely the thermodynamic concentration limit can be approached in the emitter region, and (3) the outcoupling efficiency of emitted photons into the collimating lens. Any losses from nonunity photoluminescence quantum yield can be included in this outcoupling efficiency. Each of these three factors will be discussed in detail below.

2.3 | Thermodynamic Limit From the Stokes Shift

As discussed in the introduction, the conservation of etendue requires that the ratio between the beam size before and after any passive lens is limited to the ratio of the solid angle of the beam after and before the lens. Thus, an ideal lossless lens simply trades dispersion in space (spatial entropy) for dispersion in angle (angular entropy), or vice versa, leading to a geometric gain and concentration of 1, while maintaining constant photon entropy. The geometric gain is, therefore, not only calculated by the ratio between two areas but must also include the ratio between two solid angles as shown in Equation (3)

$$G = \frac{A_{in}\Omega_{in}}{A_{out}\Omega_{out}} \tag{3}$$

This is a well-known phenomenon in optics: achieving a highly collimated beam requires a small light source (emitter), and focusing to a small spot size requires a highly collimated beam. Since perfectly diffuse light already displays maximum angular entropy, decreasing its spatial entropy (focusing to a smaller size) requires energy dissipation (entropy generation via heat). This required thermal entropy generation can be extracted from the energy difference between absorption and emission, also known as the Stokes shift. The maximum thermodynamically allowed concentration as a function of Stokes shift is given by Equation (4) [4]

$$C \leq \frac{\nu_2^2}{\nu_1^2}\exp\left(\frac{h(\nu_1 - \nu_2)}{kT}\right) \tag{4}$$

where ν_1 is the frequency of the incoming photon, ν_2 is the frequency of the emitted, redshifted photon, h is Planck's constant, k the Boltzmann constant and T is the temperature. This thermodynamic limit can be understood as the product of the entropy change due to the Stokes shift and the entropy change due to a change in the photonic density of states. The prefactor comes from the frequency dependence of the photonic density of states. Lowering the energy of photons pays the thermodynamic penalty required to reduce the etendue (reduce photon entropy). The exponential term describes the

entropy change due to the Stokes shift and has a direct analog with the electronic concentration of photogenerated carriers in a two-bandgap system. Under illumination, carriers preferentially accumulate in the lower-bandgap regions to reduce their energy. This results in a higher photogenerated carrier concentration in the lower-bandgap material, which then increases the quasi-Fermi level splitting by 60 meV per decade, while the lower carrier concentration in the surrounding high bandgap material reduces the quasi-Fermi level splitting by 60 meV per decade. which scales with the same exponential term as in Equation (4) (see Supporting Information for derivation).

Figure 2a plots the maximum concentration achievable as a function of absorption and emission wavelength (energy). Concentration factors exceeding 100 are possible with a small Stokes shift of only 0.15 eV (corresponding to 50 at 740 nm emission), while more typical Stokes shifts of 100 at 740 nm emission already correspond to maximum concentration factors above 10 000.

Although the bandgap offset determines the thermodynamic concentration limit, the carrier diffusion length of the absorbing film and size of the emitting region also set a practical limit. If the carrier diffusion length is only 1 micron, then a lens-emitter array with a period of 10 microns will be far below its thermodynamic limit. Carriers that recombine before reaching the lower-bandgap emitter region do not contribute to the generation of collimated photons, since their radiative emission occurs away from the focal point of the integrated lens. Consequently, the carrier diffusion length in the absorbing layers fundamentally constrains both the lens radius and the unit-cell pitch of the emitter–lens array. Short diffusion lengths inherently limit performance, but simply increasing the lens dimensions is also suboptimal, even when diffusion lengths are long. As the unit-cell size increases, a larger fraction of photogenerated carriers accumulates in the emitter region, potentially pushing the local carrier density into a regime where Auger recombination becomes significant, reducing the radiative efficiency.

A further practical constraint arises from the photoluminescence quantum yield: even if all photogenerated carriers successfully reach the lower-bandgap emitter, any nonradiative recombination pathways will suppress the contribution of these carriers to optical concentration. Figure 2b shows the maximum concentration factor as a function of collimating lens radius and the funneling efficiency, which takes into account both the photogenerated carrier diffusion length and the emitter photoluminescence quantum yield, using an emitter diameter of 400 nm and a Stokes shift sufficiently large that it does not limit the concentration factor. Assuming photogenerated carriers diffuse to the lower-bandgap region and recombine radiatively, they will emit at the focal point of the lens, and some fraction of the emission will be collimated by the lens. The coupling efficiency and the solid half angle of the collimating lens then provide further practical limitations to the maximum achievable concentration factor. Figure 2c plots the maximum concentration factor achieved for different outcoupling efficiency of emitted photons within a given emission half angle, combining Equation (3) with outcoupling efficiency. It is worth noting that even for low coupling efficiencies (e.g., 20%), it is possible to achieve high concentration factors ($C > 1000$) for small emission half angles (<1.15°).

3 | Simulating Performance of Real Systems

This section will introduce two designs that could be used for the proposed novel method to concentrate diffuse light, using either microlenses or micromirrors. FDTD simulations were

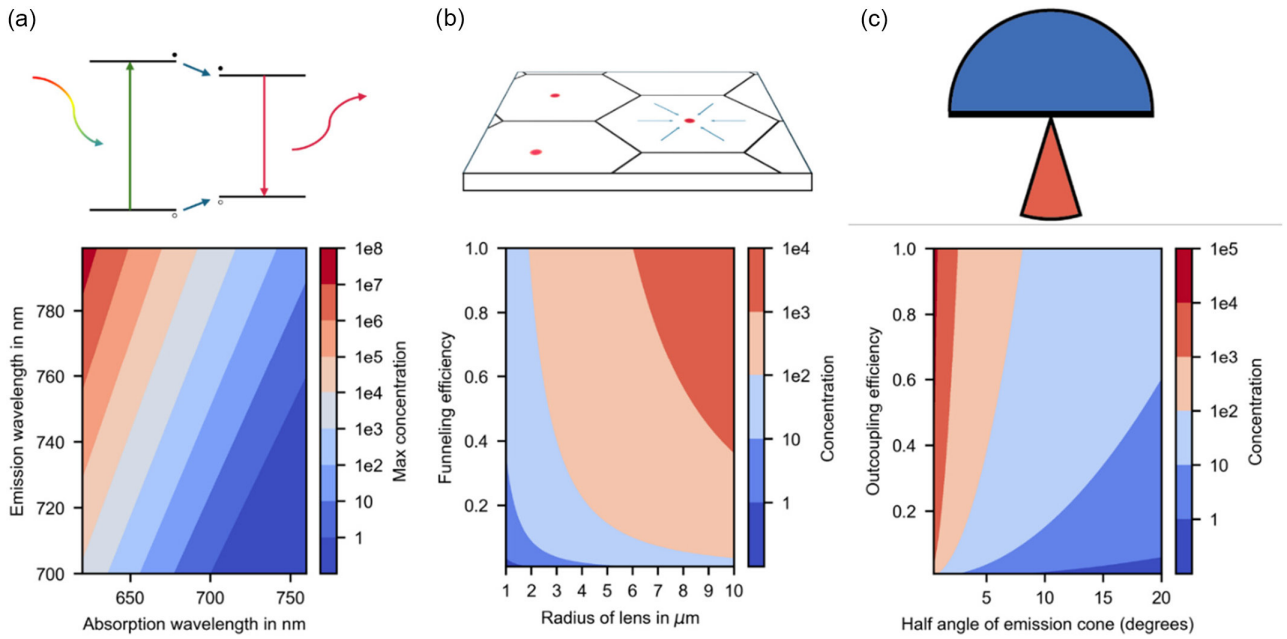

FIGURE 2 | Theoretical limits for concentration. (a) Thermodynamic concentration limit derived by Equation (1). (b) Spatial concentration achieved by funneling photogenerated carriers from high bandgap to low bandgap regions as a function of funneling radius and funneling efficiency. This plot assumes the emitter has a radius of 200 nm. (c) Concentration factor achieved by collimating emitted light within an emission cone with a certain half angle as a function of η_{out}.

conducted to show the performance with real material properties and optical geometries. The radiation pattern of the system was calculated using the open-source matlab code RETOP for the near-to-far-field transformation [50]. For the simulations, a mixed halide perovskite, namely $CH_3NH_3Pb(Br_{0.5}I_{0.5})_3$ is used as the absorber. $CH_3NH_3Pb(Br_{0.5}I_{0.5})_3$ photo-segregates under illumination into small iodide-rich regions of $CH_3NH_3Pb(Br_{0.2}I_{0.8})_3$ with a lower bandgap which act as local emitters, surrounded by a matrix with a higher bandgap. The Stokes shift, from 1.9 eV (653 nm) to 1.7 eV (729 nm), utilized in this design corresponds to a maximum concentration of ~2037×. In these simulations we assume that we can form the emitting regions selectively at the focus point of microlenses, as we have demonstrated previously [51], and that there is a way to freeze further ion diffusion or remixing after emitter formation. Notably, our design is not limited to mixed halide perovskites but could be used for any material system where a lower bandgap region could be selectively formed or aligned at the focal positions of microlens arrays. The carrier diffusion length of mixed halide perovskite ranges from 1 to 10 µm [52, 53] and the radius of the simulated microlens or micromirror (5 µm) falls within this range. Even longer effective diffusion lengths (20 µm) have been observed due to photon recycling in perovskite thin films with PLQY values (10%) well below current state-of-the-art, suggesting that the 5 µm assumption is realistically achievable [54]. The concentration factor achieved by funneling using this radius (Figures S5 and S6) falls within the thermodynamic concentration limit mentioned earlier and below the carrier density regime where Auger processes dominate. Previous research shows that the Auger-dominated regime occurs at excess carrier concentrations above $\Delta n = 10^{18}\,cm^{-3}$ [55], while the carrier densities used in our model remain well below this threshold. Under 1 sun illumination, we estimate an average excess carrier density of $\Delta n \approx 2\times10^{14}\,cm^{-3}$, assuming a uniform effective absorber thickness of 500 nm. The maximum carrier density reached through funneling, as shown in Figure S5, is $4\times10^{16}\,cm^{-3}$, which remains well below the Auger-dominated regime.

The first design makes use of the difference of refractive index between silicon dioxide and the halide perovskite. The interface between the two materials is curved and acts as a lens. Using these refractive indices, analytical calculations give the curvature and the ratio between height and width of the lens and the location of the corresponding focal point. Figure 3a shows a schematic of the design of the lens. Since the focal point differs for different refractive indices, the curvature should be adjusted when using different mixed halide perovskites or other material systems. The second design makes use of a parabolic mirror (Figure 3d). The parabolic mirror is made of aluminum and is filled with the mixed halide perovskite. The design is encapsulated by an SiO_2 layer. Since this design makes use of reflection and the light crosses the interface with normal incidence, the curvature of the parabolic mirror is uniform for different refractive indices and therefore can be applied to any material system.

4 | Results of Simulations

The optical simulations (see SI for details) first examine the electric field distribution within the two microlens designs with plane wave excitation from the top (emission direction in the final diffuse light concentrator, Figure S3a,b). According to reciprocity, the focal point will be the best position to place the emitter for maximal collimation. Indeed, the emission pattern is highly directional, with directivity values reaching over 900 for angularly averaged dipole emitters placed at the point of highest field intensity (Figure (3b,c,e,f)). Directivity in a given direction is defined as the radiated intensity in that direction divided by the average radiated intensity over all directions

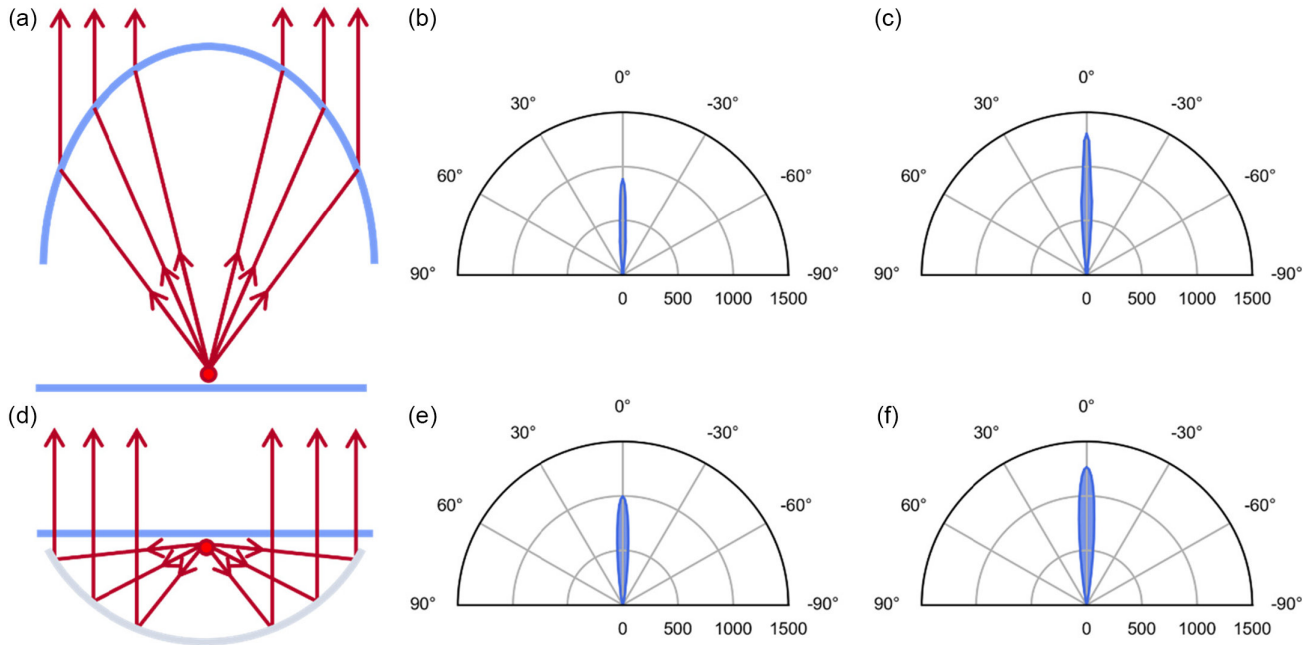

FIGURE 3 | Transmissive (a–c) and reflective (d–f) lens designs and the corresponding radiation diagrams, excluding (b,e) and including (c,f) a micromirror near the emitter. The values of the radiation patterns correspond to the directivity at the emission angle.

$$D(\theta,\varphi) = \frac{U(\theta,\varphi)}{P_{\text{rad}}/4\pi} \tag{5}$$

where U is the radiated intensity per unit solid angle and P_{rad} is total radiated power. In order to quantify the corresponding concentration limit, it is necessary to not only look at the directivity but also the outcoupling efficiency as a function of angle. Figure 4a shows the radiated power within a certain half angle, quantifying the percentage of light directed within a certain emission cone for each design (black/white lines) for emitters placed at the point of maximum intensity and at the full width half maximum (FWHM) of the focus. Figure 4b shows the concentration factor per degree half angle for the designs for emitters placed at the FWHM. The concentration factor is calculated by multiplying the geometric gain, as calculated in Equation (3), with the outcoupling efficiency, while we assume light over the full upper hemisphere is absorbed. The two designs demonstrate distinct outcoupling efficiencies; however, while the radiated power over a broader twenty-degree escape cone varies significantly between designs, the radiated power over smaller half degree angles show similar values. It is evident that the concentration decreases as the emission half angle increases.

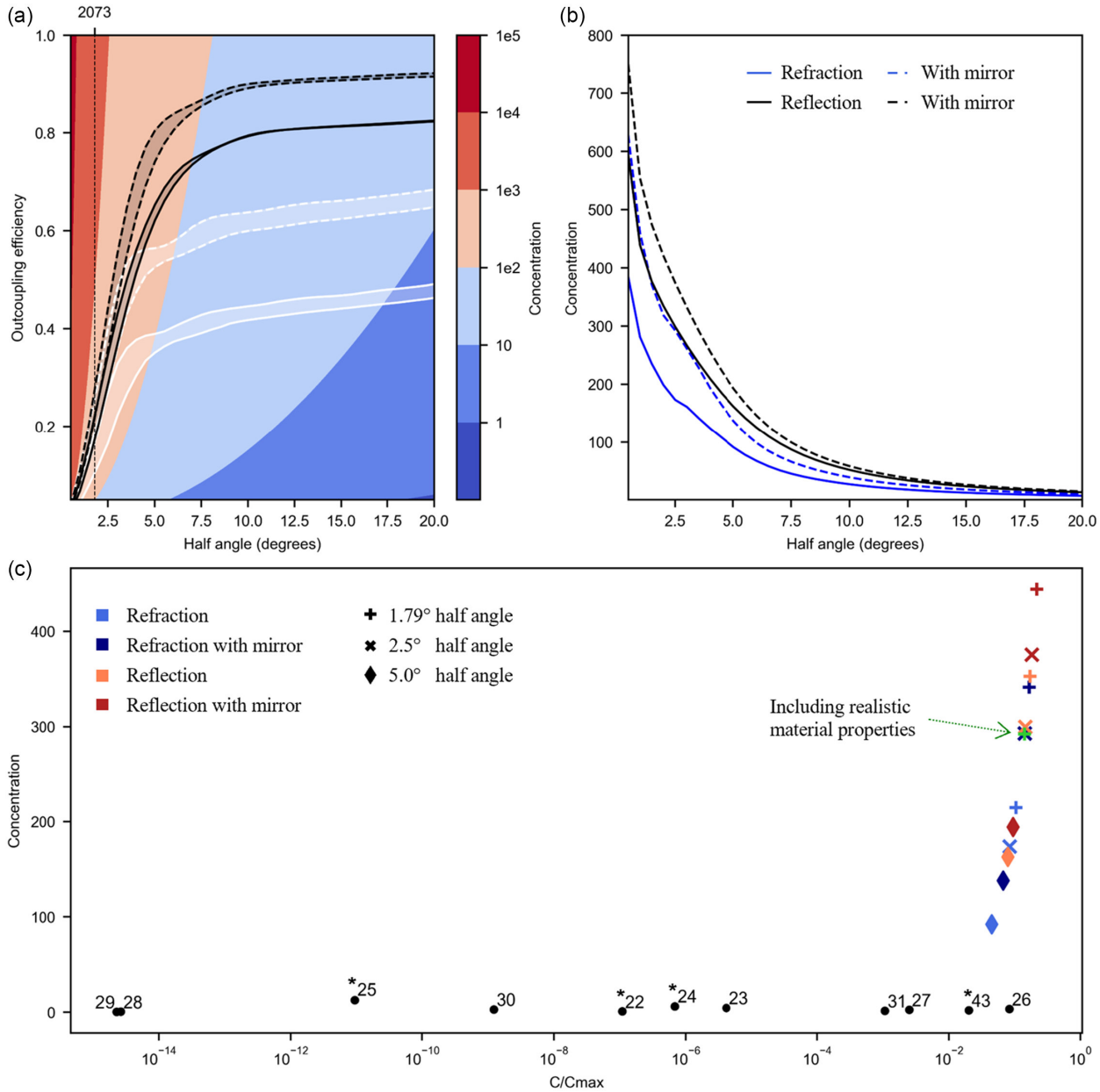

FIGURE 4 | (a) Outcoupling efficiency per half angle of the emission cone for emitters placed at the point of maximum field and at the FWHM. The continuous black and white line represent the reflective and refractive designs, respectively. The dashed lines represent the inclusion of a micromirror. The vertical dashed line illustrates the minimal outcoupling angle under a unity outcoupling efficiency. (b) The concentration factor per half angle of the emission cone of every design for emitters placed at the FWHM of the lens focus. (c) Concentration factors found in Table 1. in relation with the fraction of their theoretical limit in comparison with the concentration factors achieved in simulation for different emission half angles for emitters placed at the FWHM of the lens focus. *Values from simulations or iterations under idealized circumstances. The green plus sign demonstrates the achieved performance under reaistic conditions.

TABLE 2 | Outcoupling efficiency and concentration factor for different emission half angles for all four designs.

	Refraction				Refraction w/mirror				Reflection				Reflection w/mirror			
Angle	η_{out}		C		η_{out}		C		η_{out}		C		η_{out}		C	
1.79°	*0.187*	**0.104**	*387*	**214**	*0.257*	**0.166**	*531*	**341**	*0.220*	**0.173**	*452*	**353**	*0.274*	**0.217**	*561*	**444**
2.5°	*0.270*	**0.165**	*284*	**173**	*0.400*	**0.279**	*421*	**293**	*0.346*	**0.285**	*364*	**300**	*0.440*	**0.357**	*463*	**375**
5.0°	*0.389*	**0.350**	*102*	**92**	*0.564*	**0.525**	*149*	**138**	*0.651*	**0.619**	*171*	**163**	*0.802*	**0.738**	*211*	**194**

Values shown in italic and bold correspond to an emitter placed at the position of highest intensity and at the FWHM, respectively.

To compare the simulation results with the thermodynamic limit for concentration, it is useful to examine the concentration factor achieved at the half angle corresponding to the maximum geometric gain achievable. This occurs at a half angle of 1.79°, which corresponds to a geometric gain of 2037× (Table 2). The outcoupling efficiency at this emission cone indicates the percentage of the thermodynamic limit that can be reached. The line in Figure 4a,b marks this emission cone. The refractive and reflective designs achieve concentration factors of 214× and 353×, with outcoupling efficiencies of 10.4% and 17.3%, respectively. The performance can be enhanced by placing a micromirror just above the emitter region to improve coupling to the microlenses while only slightly reducing absorption of incoming light. Our simulations indicate that a 300 nm radius micromirror placed 30 nm above the emitting region improves the concentration factor of the refractive lens design up to 341× with a corresponding efficiency of 16.6%. The concentration factor of the reflective design even increases to 444× which is 21.7% of the thermodynamic limit. The acceptance angle of the passive focusing lens can be designed to accept any emission cone and thus tune the system depending on the application requirements. Depending on the application, it may be more important to have a higher outcoupling efficiency (convert a higher fraction of the incident photons) or reach a higher concentration factor. At an emission half angle of 5°, at which emission is still considered to be collimated, the refractive design demonstrates an outcoupling efficiency of 35.0% and 52.5%, excluding and including the micromirror, respectively. The reflective design is even better, with an outcoupling efficiency of 61.9% and 73.8% excluding and including the micromirror, respectively.

The results of these simulations assume a diffusion length of at least 5 microns. If the diffusion length will be shorter, the efficiency decreases with the square of the diffusion length. The resulting optical efficiency for shorter diffusion length is demonstrated in the Supporting Information (Figure S8a). Of course, it would make little sense to work with lenses of 5 microns if the diffusion length is shorter. Simulations were done with lens sizes that match shorter diffusion length (Figure S8b). It is clear that we get comparable results for diffusion lengths down to 3 μm (with matching lens size), with more than 50% outcoupling at 5° half angle for the champion design (Figure S9).

To assess the robustness of our design in realistic conditions, we evaluated the sensitivity of performance to variations in the emitter position and emission wavelength. Placing the emitter anywhere within the FWHM will not significantly affect the performance; however, placing it outside of the FWHM will decrease the performance (Figures S10 and S11). Moreover, shifting the emission wavelength with 50 nm results in minor changes in overall performance (Figure S12).

Finally, to demonstrate that this approach can yield record concentration factors under realistic conditions, we combine the simulated outcoupling efficiency with the calculated photoluminscent quantum yield at the core (Figures S5 and S6). As shown in Figure S13, the achievable concentration factor ranges from 18× to 350× for diffusion lengths of 5 to 30 μm, which corresponds to PLQE values of 4% to 79%, respectively. Previous research has shown that state-of-the-art halide perovskite thin films can reach a PLQE of 70% [56]. Combining this with the performance demonstrated in this work, our novel design can achieve concentration factors up to 292×, corresponding to 14% of the thermodynamic limit.

5 | Discussion/Conclusion

Conventional LSCs normally reach a geometric gain of around 10×, and the concentration factor is often only slightly above 2, even though typical thermodynamic limits taken from the Stokes shift would be at least 1000 [21]. In this work, we introduce a novel approach to concentrate diffuse light. Instead of concentrating light with an absorbing waveguide, we propose a new method based on carrier funneling and emission collimation, followed by concentration with passive optics. This new approach decreases the optical path of the emitted light drastically, significantly lowering the loss mechanisms seen in conventional luminescent concentrators. Two different designs to collimate diffuse light have been described. The first uses refraction, and the second uses reflection, to redirect light. Our new approach leads to an improvement in the diffuse light concentration by orders of magnitude, leading to concentration factors above 400× with future material improvements. Combining FDTD, transport, and recombination, simulations with realistic material property inputs demonstrate that it is currently possible to achieve concentration factors up to 292×, corresponding to 14% of the thermodynamic limit, which is an improvement of two orders of magnitude compared to current state-of-the-art with concentration values above 4.

The ultraefficient collimation of diffuse light demonstrated by this novel approach holds significant promise for any application where high-brightness and high-power light sources are useful. These could include large-area projectors, solar thermal generators, or photothermal catalytic reactors. Even many applications that currently use lasers but don't require coherence, such as laser processing, laser cutting, data transmission, and pump lasers, could benefit from this breakthrough. Just as the development of improved lenses opened up countless discoveries in microscopy

and astronomy, we expect that this leap in the performance of diffuse light concentrators can open new directions in the field of luminescent optics.

6 | Experimental Section/Methods

To test the properties of the designs, two simulations per design are done. The first simulation is to find out where the focal point will occur. In this simulation a collimated plane wave approaches the structure from the positive z-direction. The electromagnetic wave is incident along the surface normal. The electric field intensity is monitored, and the location of maximum intensity can be found. In a second simulation, an emitting dipole is placed at the point of maximum light intensity. Separate simulations are done for a dipole moment along the x-axis and for a dipole moment along the z-axis. A box is placed around the structure to retrieve the electric field data needed to calculate the far-field propagation of light. For these calculations a MATLAB package called RETOP is used. With this package we are able to interpolate the electric field values to the far-field.

For both designs it is also tested whether the inclusion of an aluminum micromirror at the interface between perovskite and the transparent medium will positively affect the results, since the light is only emitted in the hemisphere that interacts with the optic design.

For the first lensing system, different perovskite thicknesses (excluding the lens itself) were tested. The interface between perovskite and silicon oxide was placed around the analytically calculated hotspot. This was not only done to minimize the carrier funneling length but also to take advantage of possible interference between the interface and the emitter, which could result in less radiation into the bottom hemisphere.

Acknowledgments

The work was performed at the NWO institute AMOLF. E.C.G. received funding from the European Research Council (ERC). This work used the Dutch national e-infrastructure with the support of the SURF Cooperative using grant no. EINF-13617.

Funding

This work was supported by the European Research Council (ERC) Consolidator (Grant 101043783).

Conflicts of Interest

The authors declare no conflicts of interest.

Data Availability Statement

The data that support the findings of this study are available from the corresponding author upon reasonable request.

References

1. G. Galilei, "Sidereus nuncius (trans. Van Helden, A.)," (University of Chicago Press, 1989).

2. L. A. Robertson, "Antoni van Leeuwenhoek 1723–2023: a review to commemorate Van Leeuwenhoek's death, 300 years ago," *Antonie Van Leeuwenhoek* 116 (2023): 919–935.

3. G. P. Agrawal, "Nonlinear Science at the Dawn of the 21st Century," (Springer, 2000), 195–211.

4. E. Yablonovitch, "Thermodynamics of the Fluorescent Planar Concen trator," *Journal of the Optical Society of America* 70 (1980): 1362–1363.

5. M. Debije, "Better Luminescent Solar Panels in Prospect," *Nature* 519 (2015): 298–299.

6. L. H. Slooff, E. E. Bende, A. R. Burgers, et al., "A Luminescent Solar Concentrator with 7.1% Power Conversion Efficiency," *Physica status solidi (RRL) – Rapid Research Letters* 2 (2008): 257–259.

7. I. Papakonstantinou, M. Portnoi, and M. G. Debije, "The Hidden Potential of Luminescent Solar Concentrators," *Advanced Energy Materials* 11 (2021): 2002883, https://doi.org/10.1002/aenm.202002883.

8. F. Meinardi, F. Bruni, and S. Brovelli, "Luminescent Solar Concentrators for Building-Integrated Photovoltaics," *Nature Reviews Materials* 2 (2017): 17072, https://doi.org/10.1038/natrevmats.2017.72.

9. M. G. Debije and P. P. C. Verbunt, "Thirty Years of Luminescent Solar Concentrator Research: Solar Energy for the Built Environment," *Advanced Energy Materials* 2 (2012): 12–35.

10. T. A. de Bruin and W. G. J. H. M. van Sark, "Shining Lights on Limits: Optimizing Luminescent Solar Concentrators for Solar Windows," *Advanced Photonics Research* 6 (2025): 2400068.

11. M. Cao, X. Zhao, and X. Gong, "Achieving High-Efficiency Large-Area Luminescent Solar Concentrators," *JACS Au* 3 (2023): 25–35.

12. F. Meinardi, Q. A. Akkerman, F. Bruni, et al., "Doped Halide Perovskite Nanocrystals for Reabsorption-Free Luminescent Solar Concentrators," *ACS Energy Letters* 2 (2017): 2368–2377.

13. J. Sathian, J. D. Breeze, B. Richards, N. M. Alford, and M. Oxborrow, "Solid-State Source of Intense Yellow Light Based on a Ce: YAG Luminescent Concentrator," *Optics Express* 25 (2017): 13714–13727.

14. P. Pichon, A. Barbet, J.-P. Blanchot, et al., "Light-Emitting Diodes: A New Paradigm for Ti: Sapphire Pumping," *Optica* 5 (2018): 1236.

15. D. K. G. de Boer, D. Bruls, and H. Jagt, "High-Brightness Source Based on Luminescent Concentration," *Optics Express* 24 (2016): A1069.

16. J. Roncali, "Luminescent Solar Collectors: Quo Vadis?," *Advanced Energy Materials* 10 (2020): 2001907, https://doi.org/10.1002/aenm.202001907.

17. C. Tummeltshammer, A. Taylor, A. J. Kenyon, and I. Papakonstantinou, "Losses in Luminescent Solar Concentrators Unveiled," *Solar Energy Materials and Solar Cells* 144 (2016): 40–47.

18. W. H. Weber and J. Lambe, "Luminescent Greenhouse Collector for Solar Radiation," *Applied Optics* 15 (1976): 2299.

19. T. K. Baikie, J. Xiao, B. H. Drummond, N. C. Greenham, and A. Rao, "Spatially Resolved Optical Efficiency Measurements of Luminescent Solar Concentrators," *ACS Photonics* 10 (2023): 2886–2893.

20. T. K. Baikie, B. Daiber, E. Kensington, et al., "Revealing the Potential of Luminescent Solar Concentrators in Real-World Environments," *Joule* 8 (2024): 799–816.

21. S. Castelletto and A. Boretti, "Luminescence Solar Concentrators: A Technology Update," *Nano Energy* 109 (2023): 108269.

22. F. Meinardi, S. Ehrenberg, L. Dhamo, et al., "Highly Efficient Luminescent Solar Concentrators Based on Earth-Abundant Indirect-Bandgap Silicon Quantum Dots," *Nature Photonics* 11 (2017): 177–185.

23. F. Meinardi, A. Colombo, K. A. Velizhanin, et al., "Large-Area Luminescent Solar Concentrators Based on Stokes-Shift-Engineered Nanocrystals in a Mass-Polymerized PMMA Matrix," *Nature Photonics* 8 (2014): 392–399.

24. F. Meinardi, H. McDaniel, F. Carulli, et al., "Highly Efficient Large-Area Colourless Luminescent Solar Concentrators Using Heavy-Metal-Free Colloidal Quantum Dots," *Nature Nanotechnology* 10 (2015): 878–885.

25. H. Li, K. Wu, J. Lim, H. J. Song, and V. I. Klimov, "Doctor-Blade Deposition of Quantum Dots onto Standard Window Glass for Low-Loss Large-Area Luminescent Solar Concentrators," *Nature Energy* 1 (2016): 1–9.

26. M. Wei, F. Pelayo García de Arquer, G. Walters, et al., "Ultrafast Narrowband Exciton Routing Within Layered Perovskite Nanoplatelets Enables Low-Loss Luminescent Solar Concentrators," *Nature Energy* 4 (2019): 197–205.

27. Y. Zhou, D. Benetti, Z. Fan, et al., "Near Infrared, Highly Efficient Luminescent Solar Concentrators," *Advanced Energy Materials* 6 (2016): 1501913.

28. C. Li, W. Chen, D. Wu, et al., "Large Stokes Shift and High Efficiency Luminescent Solar Concentrator Incorporated with $CuInS_2$/ZnS Quantum Dots," *Scientific Reports* 5 (2015): 17777.

29. J. Li, H. Zhao, X. Zhao, and X. Gong, "Boosting Efficiency of Luminescent Solar Concentrators Using Ultra-Bright Carbon Dots with Large Stokes Shift," *Nanoscale Horizons* 8 (2022): 83–94.

30. M. R. Bergren, N. S. Makarov, K. Ramasamy, et al., "High-Performance $CuInS_2$ Quantum Dot Laminated Glass Luminescent Solar Concentrators for Windows," *ACS Energy Letters* 3 (2018): 520–525.

31. Z. Krumer, W. G. J. H. M. van Sark, R. E. I. Schropp, and C. de Mello Donegá, "Compensation of Self-Absorption Losses in Luminescent Solar Concentrators by Increasing Luminophore Concentration," *Solar Energy Materials and Solar Cells* 167 (2017): 133–139.

32. R. Paniagua-Domínguez, Y. F. Yu, E. Khaidarov, et al., "A Metalens with a Near-Unity Numerical Aperture," *Nano Letters* 18 (2018): 2124–2132.

33. Y.-Q. Liu, J. Sun, Y. Shu, et al., "High Numerical Aperture and Large Focusing Efficiency Metalens Based on Multilayer Transmitarray Elements," *Optics and Lasers in Engineering* 147 (2021): 106734.

34. L. M. Einhaus, G. C. Heres, J. Westerhof, et al., "Free-Space Diffused Light Collimation and Concentration," *ACS Photonics* 10 (2023): 508–517.

35. A. Goetzberger and W. Greubel, "Solar Energy Conversion with Fluorescent Collectors," *Applied Physics* 14 (1977): 123.

36. L. A. Weinstein, J. Loomis, B. Bhatia, et al., "Concentrating Solar Power,"*Chemical reviews* 115 (2015): 12797–12838.

37. C. Cruciano, D. Rocco, A. Genco, et al., "Shaping the Emission Directivity of Single Quantum Dots in Dielectric Nanodisks Exploiting Mie Resonances," *ACS Nano* 19 (2025): 3500–3509.

38. T. Veeken, B. Daiber, H. Agrawal, et al., "Directional Quantum Dot Emission by Soft-Stamping on Silicon Mie Resonators," *Nanoscale Advances* 4 (2022): 1088–1097.

39. M. Jeong, B. Ko, C. Jung, et al., "Printable Light-Emitting Metasurfaces with Enhanced Directional Photoluminescence," *Nano Letters* 24 (2024): 5783–5790.

40. H. Yang, W. Mills, S. Bharadwaj, et al., "Orchestrating Spontaneous Emission with Metasurfaces: Recent Advances in Engineering Thermal, Luminescent, and Quantum Emissions," *Advanced Optical Materials* 13 (2025): 2402755, https://doi.org/10.1002/adom.202402755.

41. Y. Chung, G. Baek, J. Min, et al., "Tailoring Directional Emission of Colloidal Quantum Dots via Mode Coupling with Photonic Crystals," *Nanoscale* 17 (2025): 20880–20888.

42. Y. Chen, J. Liu, J. Hu, et al., "Vertical Emission of Blue Light from a Symmetry-Breaking Plasmonic Nanocavity–emitter System Supporting Bound States in the Continuum," *Advanced Functional Materials* 35 (2025): 2500133.

43. S. Wang, Q. Le-Van, T. Peyronel, et al., "Plasmonic Nanoantenna Arrays as Efficient Etendue Reducers for Optical Detection," *ACS Photonics* 5 (2018): 2478–2485.

44. B. Zhang, G. Lyu, E. A. Kelly, et al., "Förster Resonance Energy Transfer in Luminescent Solar Concentrators," *Advancement of Science* 9 (2022): 220.

45. X. Dai, Z. Zhang, Y. Jin, et al., "Solution-Processed, High-Performance Light-Emitting Diodes Based on Quantum Dots," *Nature* 515 (2014): 96–99.

46. H. Shen, Q. Gao, Y. Zhang, et al., "Visible Quantum Dot Light-Emitting Diodes with Simultaneous High Brightness and Efficiency," *Nature Photonics* 13 (2019): 192–197.

47. D. Vasudevan, R. R. Gaddam, A. Trinchi, and I. Cole, "Core–shell Quantum Dots: Properties and Applications," *Journal of Alloys and Compounds* 636 (2015): 395–404.

48. E. T. Hoke, D. J. Slotcavage, E. R. Dohner, et al., "Reversible Photo-Induced Trap Formation in Mixed-Halide Hybrid Perovskites for Photovoltaics," *Chemical Science* 6 (2015): 613–617.

49. J. S. Van der Burgt, S. A. Rigter, N. De, G. Fortman, and E. C. Garnett, "Self-Tracking Solar Concentrator with Absorption of Diffuse Sunlight," *Advanced Optical Materials* 11 (2023): 2202013.

50. J. Yang, J. P. Hugonin, and P. Lalanne, "Near-to-Far Field Transformations for Radiative and Guided Waves," *ACS Photonics* 3 (2016): 395–402.

51. J. S. van der Burgt, et al., "Perovskite Plasticity: Exploiting Instability for Self-Optimized Performance," *Advanced Functional Materials* 32, 2022.

52. Z. Guo, J. S. Manser, Y. Wan, P. V. Kamat, and L. Huang, "Spatial and Temporal Imaging of Long-Range Charge Transport in Perovskite Thin Films by Ultrafast Microscopy," *Nature Communications* 6 (2015): 7471.

53. Y. Zhao, A. M. Nardes, and K. Zhu, "Solid-State Mesostructured Perovskite $CH_3NH_3PbI_3$ Solar Cells: Charge Transport, Recombination, and Diffusion Length," *Journal of Physical Chemistry Letters* 5 (2014): 490–494.

54. L. M. Pazos-Outón, M. Szumilo, R. Lamboll, et al., "Photon Recycling in Lead Iodide Perovskite Solar Cells," *Science* 351 (2016): 1430–1433.

55. S. C. Gillespie, J. Gautier, J. S. Van Der Burgt, et al., "Silicon-Inspired Analysis of Interfacial Recombination in Perovskite Photovoltaics," *Advanced Energy Materials* 14 (2024): 2400965.

56. L. Wang, Z. Y. Ooi, F.-Y. Jia, et al., "Efficient Perovskite LEDs with Tailored Atomic Layer Number Emission at Fixed Wavelengths," *Science Advances* 11 (2025): eadp9595.

Supporting Information

Additional supporting information can be found online in the Supporting Information section.